Wind-Forced Seasonal Exchange between Marginal Seas and the Open Ocean

MICHAEL A. SPALL®

^a Woods Hole Oceanographic Institution, Woods Hole, Massachusetts

(Manuscript received 13 July 2022, in final form 21 November 2022)

ABSTRACT: The circulation within marginal seas subject to periodic winds, and their exchange with the open ocean, are explored using idealized numerical models and theory. This is motivated by the strong seasonal cycle in winds over the Nordic Seas and the exchange with the subpolar North Atlantic Ocean through the Denmark Strait and Faroe Bank Channel. Two distinct regimes are identified: an interior with closed f/h contours and a shallow shelf region that connects to the open ocean. The interior develops a strong oscillating along-topography circulation with weaker ageostrophic radial flows. The relative importance of the bottom Ekman layer and interior ageostrophic flows depends only on $\omega h/C_d$, where ω is the forcing frequency, h is the bottom depth, and C_d is a linear bottom drag coefficient. The dynamics on the shelf are controlled by the frictional decay of coastal waves over an along-shelf scale $L_y = f_0 L_s H_s/C_d$, where f_0 is the Coriolis parameter, and L_s and H_s are the shelf width and depth. For L_y much less than the perimeter of the basin, the surface Ekman transport is provided primarily by overturning within the marginal sea and there is little exchange with the open ocean. For L_y on the order of the basin perimeter or larger, most of the Ekman transport is provided from outside the marginal sea with an opposite exchange through the deep part of the strait. This demonstrates a direct connection between the dynamics of coastal waves on the shelf and the exchange of deep waters through the strait, some of which is derived from below sill depth.

SIGNIFICANCE STATEMENT: The purpose of this study is to understand how winds over marginal seas, which are semienclosed bodies of water around the perimeter of ocean basins, can force an exchange of water, heat, salt, and other tracers through narrow straits between the marginal sea and the open ocean. Understanding this exchange is important because marginal seas are often regions of net heat, freshwater, and carbon exchange with the atmosphere. The present results identify a direct connection between processes along the coast of the marginal sea and the flow of waters through deep straits into the open ocean.

KEYWORDS: Coastal flows; Ekman pumping/transport; Ocean circulation

1. Introduction

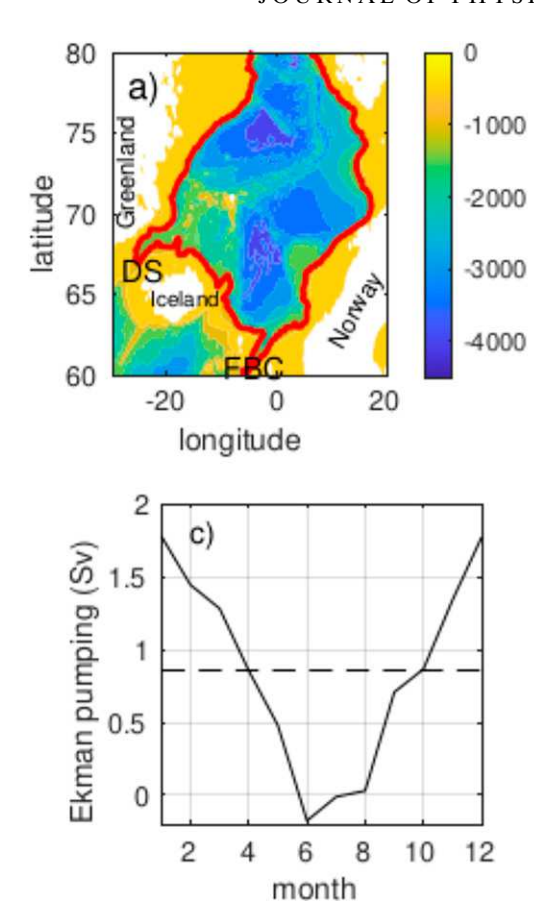
Marginal seas are defined as a portion of the ocean that is partially enclosed by islands, archipelagos, or peninsulas and lies adjacent to the open ocean. They are typically also bounded by submarine ridges, sometimes with narrow and/or shallow straits connecting the marginal sea to the open ocean. For straits with a shallow sill depth, much of the region within the marginal sea is characterized by closed contours of f/h, where fis the Coriolis parameter and h is the bottom depth. Because marginal seas are also located adjacent to continents, they are generally subject to strong buoyancy- and wind-forcing on seasonal time scales. Much previous work has focused on the seasonal water mass transformation in marginal seas that experience buoyancy-forced deep convection (Marshall and Schott 1999; Spall 2004; Straneo 2006). The present focus is on the wind-forced overturning circulation and exchange with the open ocean.

Although the approach taken here is very idealized in nature, the problem is motivated by the circulation within the Nordic Seas and the exchange with the subpolar North Atlantic Ocean through Denmark Strait and the Faroe Bank Channel (FBC). The bottom topography of the Nordic Seas is shown in

Corresponding author: Michael A. Spall, mspall@whoi.edu

Fig. 1a, with the relevant geographical features and the 850-m isobath indicated. The sill depth within the Denmark Strait is approximately 650 m and that in the FBC is approximately 850 m. Thus, the region deeper than 850 m has no direct connection to lower latitudes while depths shallower than that can connect to the subpolar North Atlantic along contours of constant f/h. This distinction provides the basis for much of the theoretical development below. The daily Ekman pumping rate from the ERA5 reanalysis (Hersbach et al. 2020) integrated within the 850-m isobath is shown in Fig. 1b for the period 2000-20 (positive upward). The upwelling into the Ekman layer during extreme high-frequency events exceeds 10 Sv $(1 \text{ Sy} \equiv 10^6 \text{ m}^3 \text{ s}^{-1})$. There is also a clear seasonal cycle with maximum upwelling in winter and near zero net Ekman pumping in summer. The monthly mean over this 20-yr period is shown in Fig. 1c. The maximum upwelling is about 1.8 Sv in winter and close to zero in summer with an annual mean of 0.87 Sv. This framework of closed f/h contours in the interior, open f/h contours extending outside the marginal sea, and a net Ekman pumping on seasonal time scales provides the basis for the idealized configurations used here.

Nøst and Isachsen (2003) applied a circulation integral along contours of constant f/h to estimate the circulation forced by mean winds in the Nordic Seas and Arctic Ocean. They found that wind stress along any stretch of a contour would force circulation all along the contour, sometimes



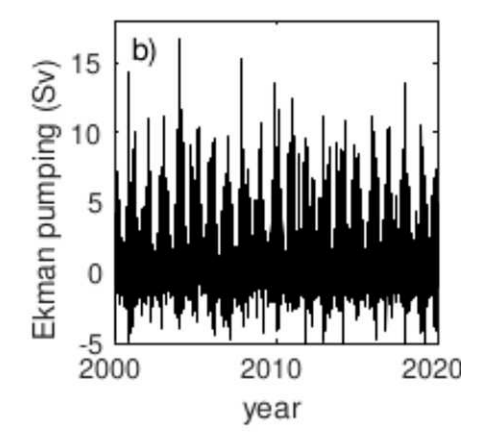


FIG. 1. (a) Bottom topography in the Nordic Seas with Denmark Strait (DS) and Faroe Bank Channel (FBC) indicated. The 850-m isobath is indicated in red. (b) Daily Ekman pumping integrated within the 850-m isobath from ERA5 reanalysis from 2000 through 2020. (c) Monthly mean from (b). The dashed line indicates the annual mean of 0.87 Sv.

extending thousands of kilometers from the region of forcing. The mean along-contour flow in this steady case produces a transport in the bottom boundary layer that balances the surface Ekman transport into or out of the closed contour. A similar constraint was applied by Kamenkovich (1962) in the Southern Ocean. Isachsen et al. (2003) considered timedependent winds, which results in a mismatch between surface and bottom Ekman layer transports and time-dependent sea surface height (ssh) within, and currents along, the closed contours. This simple barotropic model was able to reproduce fairly well current meter observations and results from a more comprehensive numerical model. Spall (2016) found that the barotropic theory was a good approximation even for stratified flows for forcing periods short relative to the time it takes a baroclinic Rossby wave to cross the region of closed f/h contours. For the Nordic Seas, the first mode baroclinic deformation radius is O(8) km (Nurser and Bacon 2013), which gives a Rossby wave phase speed of $O(10^{-3})$ m s⁻¹ and a basincrossing time scale of O(10-20) years. So it is anticipated that for seasonal time scales the primary response to winds will be barotropic, consistent with Isachsen et al. (2003).

A seasonal cycle in the FBC overflow of 0.2–0.4 Sv has been observed (Hansen and Østerhus 2007; Hansen et al. 2015; Chafik et al. 2020) with a maximum overflow strength in summer to fall and a minimum in winter to spring. Bringedal et al. (2018) find a similar seasonal cycle in both the FBC

overflow and the inflow of lighter waters through Denmark Strait. Correlations with atmospheric forcing fields and a simple model were used to attribute this seasonality primarily to seasonal variability in the winds over the Nordic Seas and around Iceland. Köhl et al. (2007) also find that wind-forcing around Iceland on seasonal time scales drives variability in the barotropic exchange through Denmark Strait.

It is likely that the Denmark Strait and Faroe Bank Channel overflows are, at least at times, hydraulically controlled (Whitehead et al. 1974; Pratt and Whitehead 2008). Pratt (1997) and Helfrich and Pratt (2003) studied the connection between the geostrophic flow in an upstream basin forced by a steady mass source and a hydraulically controlled flow over a sill. It was shown that the circulation and the mean stratification within the upstream basin were dependent on where mass was introduced into the basin (interior or boundary), but the flow through the strait was nearly independent of the source. Helfrich (1995) applied a barotropic, periodic external forcing to a two-layer hydraulically controlled exchange flow. He found that for weak forcing (perturbation velocity is small relative to the baroclinic gravity wave speed) the exchange through the strait was close to the linear sum of the steadyforced flow plus the time-dependent perturbation forced flow, independent of the forcing frequency.

Several previous studies considered the circulation along closed *flh* contours while the present study seeks to connect

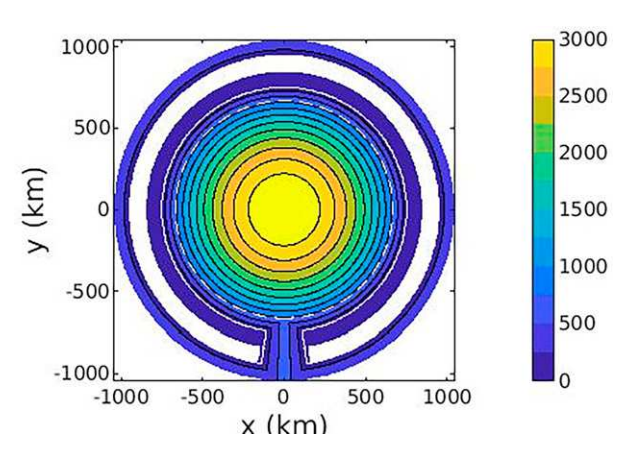


FIG. 2. The model domain and bottom topography (colors). This example consists of a deep basin surrounded by a shallow shelf with one strait connecting the marginal sea to the outer restoring region (outermost 100 km of the domain). The wind stress curl is uniform within the dashed white circle at $R_c = 668$ km and is zero outside the circle. The shelf break is at $R_i = 750$ km and is indicated by the thinner solid white line.

these interior dynamics to flow through straits that extend outside the marginal sea. The connections between wind forcing, coastal waves, and the exchange of deep waters through straits connecting marginal seas with the open ocean will be explored using an idealized configuration of a primitive equation ocean model and simple analytic models representing the interior and coastal regions of the marginal sea. The numerical model is carefully designed to understand how variable winds within the marginal sea can force exchange. This is distinct and separate from exchange that might be forced from variable winds outside the marginal sea. This approach allows for identification of the controlling nondimensional parameters and facilitates a conceptual understanding of how the basin responds to local time-dependent winds.

2. Examples with a primitive equation model

a. Model configuration

The numerical model used in this study is the *z*-coordinate, hydrostatic version of the MITgcm (Marshall et al. 1997). The model solves the primitive equations of motion on a staggered *C* grid in the horizontal and fixed depth coordinates in the vertical with a partial cell treatment of the bottom topography. A linear equation of state is used as $\rho = \rho_0 + \alpha T$, where ρ_0 is a reference density, *T* is temperature, and $\alpha = -0.2 \text{ kg m}^{-3} \text{ C}^{-1}$.

Subgrid-scale processes are parameterized with the deformation-dependent Smagorinsky horizontal Laplacian viscosity (Smagorinsky 1963) with nondimensional coefficient 3.0. Vertical viscosity and diffusivity are also second order, with coefficients 10^{-4} m² s⁻¹ and 10^{-5} m² s⁻¹, respectively. There is no explicit horizontal diffusion. There is also a linear bottom drag with coefficient 5×10^{-4} m s⁻¹, which is the value found by Isachsen et al. (2003) to best reproduce observed variability in a regional model of the wind-forced Nordic Seas. The bottom drag turns out to be a key parameter

of the system and the sensitivity of the solutions to the bottom drag coefficient will be discussed. Calculations carried out with quadratic bottom drag produce similar results for parameter values with similar spindown time scales, so the general conclusions are not sensitive to the form of bottom friction.

The model domain is an idealized representation of a semienclosed marginal sea with a sloping bottom surrounded by a shelf (Fig. 2). Because our primary motivation is the highlatitude Nordic Seas at annual forcing periods, the model is configured on an f plane. The example calculation described here was repeated on a β plane with $\beta = 2 \times 10^{-11} \text{ m}^{-1} \text{ s}^{-1}$ and produced essentially identical results. The baroclinic Rossby waves are too slow at this latitude to be important on seasonal time scales. The model domain is circular with a radius of 1050 km and a grid spacing of 5 km. The baroclinic deformation radius in the interior is approximately 25-30 km and is well resolved by the model grid. The deformation radius on the shelf is 10 km and is only marginally resolved. Because the response at these frequencies is dominated by the barotropic mode, the results are not sensitive to the stratification. The configuration represents a marginal sea with radius $R_m = 850$ km, a 100-km-wide boundary (white region), and a 100-km-wide restoring region outside the marginal sea. In the restoring region, the velocity field is restored toward zero and the density field is restored toward the initial stratification with a time scale of 5 days. This is intended to prevent signals from propagating around the basin and reentering the marginal sea through the strait. This initial example has only one strait but multiple straits will be considered later. The maximum basin depth is 3000 m, and the sill depth is 650 m, so there is a region of closed f/h contours and a region where f/hcontours connect to the restoring region. The shelf is 100 m deep and 100 km wide (these will be varied later).

The bottom depth in the interior is defined as

$$h = H_m + (H_s - H_m)R^2/R_i^2, (1)$$

where $H_m = 3000$ m is the maximum bottom depth, $H_s = 100$ m is the shelf depth, R is the radius, and $R_i = 750$ km is the radius of the sloping bottom. For $R > R_i$ the bottom depth is H_s . This provides a smoothly varying bottom depth, which will allow for analysis to be carried out along closed f/h contours. There are 60 levels in the vertical direction, with a grid spacing expanding from 5 m at the surface to 200 m near H_m .

The model is forced by periodic winds in the azimuthal direction that oscillate with frequency ω and have zero mean. The central calculation discussed below was repeated with the periodic oscillations plus a mean cyclonic wind stress curl over the basin for a period of 34 years, resulting in a mean cyclonic circulation within the basin of approximately 10 Sv and a mean Ekman suction of 0.4 Sv. The seasonal cycle of the exchange through the strait was nearly identical to that produced for a calculation with no mean wind stress curl. Thus, the circulation produced by the periodic oscillations should be viewed as perturbations to the mean wind- and buoyancy-driven circulation in the marginal sea. The winds are designed such that the wind stress curl produces uniform Ekman pumping in the regions where the depth exceeds $H_c = 700$ m

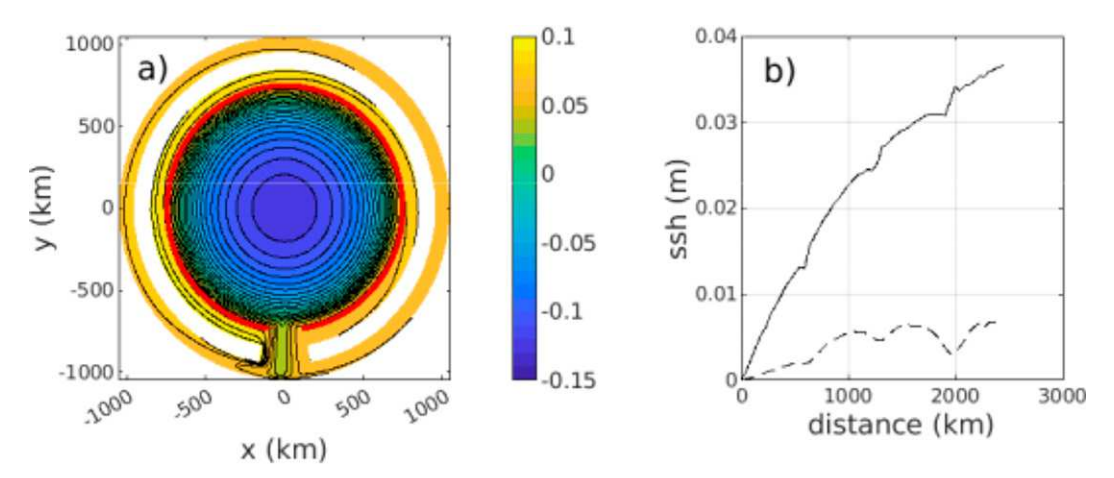


FIG. 3. (a) Sea surface height (m) from the model at 90-days integration for a forcing period of P = 360 days. The red circle marks the shelf break. (b) Sea surface height (relative to the right-hand side of the channel) around the perimeter (solid line) and around the shelf break (dashed line).

(at $R_c = 668$ km) and zero Ekman pumping at shallower depths. This transition depth was chosen to assure that there was no Ekman pumping directly onto contours that pass through the strait, which could force exchange. While this may be an interesting and important forcing mechanism, the intent here is to isolate the effects of wind stress curl in the region of closed f/h contours. The wind stress in the azimuthal direction is defined as

$$\tau(r,t) = \gamma R \sin \omega t$$
 for $R < R_c$
$$\tau(r,t) = \gamma (R_c^2/R) \sin \omega t$$
 for $R \ge R_c$. (2)

The second expression maintains a constant radial Ekman transport so that the Ekman pumping is zero for $R \ge R_c$. This was done so that the circulation on the shelf is that forced only by the interaction of the wind stress with the boundary. The scaling constant $\gamma = 2.8 \times 10^{-8} \, \mathrm{N \ m^{-3}}$. This gives a maximum wind stress at radius R_c of 0.019 N m⁻² and a maximum Ekman pumping/suction of ± 0.78 Sv. The wind within the restoring region is set to zero if it is outside the azimuthal range of any of the straits. This maintains zero wind stress curl and also prevents forcing coastal waves from the interaction of winds parallel to the inner boundary of the restoring region. If such waves were generated, they would propagate into the marginal sea and introduce an outside source of variability.

The initial stratification is exponential, defined as

$$T(z) = T_b + (T_s - T_b)e^{-z/z_0}, (3)$$

where $T_b = 0$ is the bottom temperature, $T_s = 10^{\circ}\text{C}$ is the surface temperature, and $z_0 = 1000$ m is a vertical decay scale. The solutions are not very sensitive to the initial stratification but this is chosen to be representative of the Norwegian Sea. The temperature in the marginal sea is restored toward this initial stratification with a time scale of 90 days. This is intended to represent buoyancy-forcing and mixing processes that maintain the stratification and are absent from this model.

The model is initialized at rest and run for 4 years with a period of 360 days (1440 days). Most of the following analysis is based on an average of the seasonal cycle over the final 2 years of integration. The general circulation response and the two different flow regimes are evident from the sea surface height at 810 days of integration, which is when the wind stress is at its maximum strength (Fig. 3). In the region of closed f/h contours there is a strong cyclonic circulation with a sea surface height anomaly at the center of the basin of -0.13 m and a transport streamfunction of 16.7 Sv. The azimuthal flow in the interior is along f/h contours and is nearly barotropic. The red circle marks the edge of the shelf. Just offshore from this, and shallower than the sill depth, the flow follows the topographic contours into and out of the strait, also flowing largely along f/h contours. However, on the shelf there is the development of a gradient in ssh across the shelf. At the eastern side of the strait, ssh on the shelf is nearly uniform. Progressing cyclonically around the basin, the ssh on the boundary increases such that by the time one reaches the western side of the strait there is an ssh change across the shelf of several centimeters (Fig. 3b). The ssh along the shelf break is nearly constant around the perimeter of the basin. This also results in a net change in ssh across the strait, which implies that there is a net geostrophic flow at the surface that is directed from the marginal sea out of the strait. A major focus of the subsequent analysis is to understand what controls this wind-forced exchange.

The interior flow is dominated by the strong recirculation along closed f/h contours, which is to leading order geostrophic and barotropic. This is shown by the azimuthally averaged velocity along contours of constant f/h in Fig. 4a. This diagnostic only goes as shallow as the sill depth, which marks the boundary of the region of closed interior f/h contours. The tangential velocity in the deep basin is weak and increases with increasing radius to a maximum of about $0.06~{\rm m~s^{-1}}$ at the rim of the closed f/h contours. The velocity rapidly decreases to zero in the thin bottom Ekman layer. There is also an ageostrophic overturning in the radial

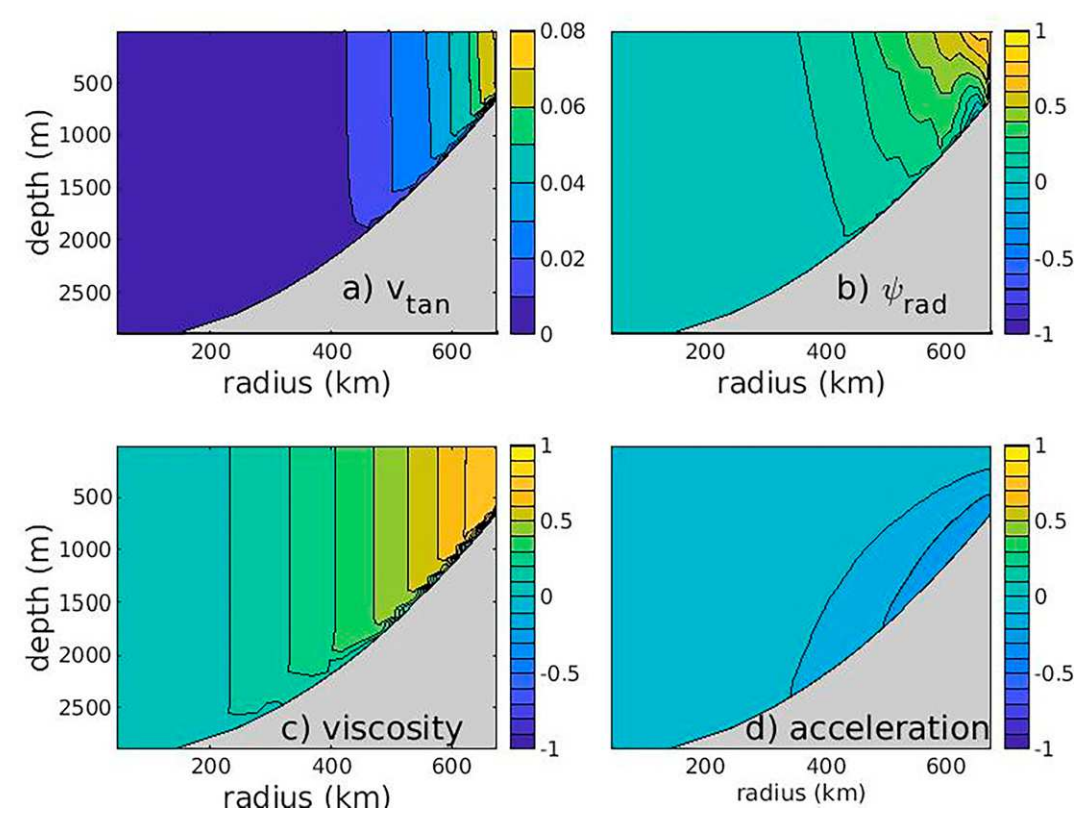


FIG. 4. At 90 days of integration (time = P/4): (a) tangential velocity (m s⁻¹) and (b) radial overturning streamfunction ψ_{rad} (Sv). Also shown are contributions to ψ_{rad} from (c) viscosity and (d) acceleration (Sv).

direction. The radial overturning was calculated along depth contours by integrating the radial velocity from the surface to the bottom. The general pattern of overturning is indicated on day 90 (Fig. 4b). The sign of course oscillates in time as the wind stress anomaly changes sign but the overturning at this time provides a useful illustration of the dominant effects. Water is being drawn into the surface Ekman layer with the vertical transport increasing with radius, as the surface area increases. This radial transport is provided primarily near the bottom in the deep basin but also throughout the water column as one moves onshore.

The terms responsible for this radial transport can be identified by rotating each term in the momentum equations into the azimuthal direction, dividing by the Coriolis parameter, and then integrating in both the azimuthal direction and from the surface to the bottom. The pressure gradient and the geostrophic radial velocity integrate to zero, leaving the ageostrophic radial velocity and the terms that balance it. These can be represented as viscous terms (surface stress, bottom drag, lateral friction), acceleration of the azimuthal velocity, and nonlinear terms (Reynolds stresses). The nonlinear terms were found to be small and will not be discussed further. Viscous and time-dependent terms are plotted in Figs. 4c and 4d. The frictional term is contained primarily near the surface and bottom (Fig. 4c), where it supports a radial ageostrophic flow. If the flow were steady and linear, all the transport into

the surface Ekman layer would be provided by a vertical transport extending from the bottom boundary layer. However, the flow is time dependent, and the acceleration term is important (Fig. 4d). It is balancing a radial flow directed from the perimeter toward the interior, in the same direction as the bottom boundary layer. This is responsible for the interior radial flow seen in Fig. 4b.

The flow on the shelf is dominated by an oscillating alongshelf flow of several cm s⁻¹, as indicated by the cross-shelf average of the along-shelf flow taken at y = 0 on the western side of the basin, shown in Fig. 5a. The flow is nearly uniform across the shelf, so this is representative of the flow everywhere on the shelf. Uniform flow across the shelf is consistent with the analytic wind-forced flat-shelf solutions of Csanady (1978). The current is nearly barotropic except for near the bottom where there is a decrease toward zero in the bottom Ekman layer. The cross-shelf flow is dominated by the surface Ekman layer, which oscillates with an amplitude of about 5 cm s⁻¹, or an overturning strength of 0.2 m² s⁻¹ per unit along-shelf distance. There is a flow in the bottom Ekman layer directed in the opposite direction. At this location its depth integrated transport nearly balances the surface Ekman transport (to within 10%). The cross-shelf flow at middepth shows an asymmetry with very weak offshore flow during times of coastal downwelling (0 < t < 0.5 yr) and weak, but not insignificant, onshore flow during times of coastal

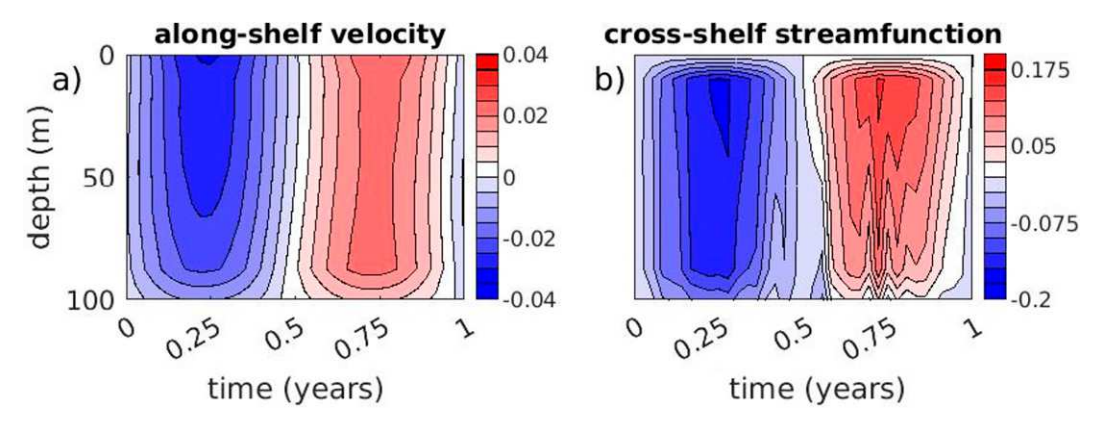


FIG. 5. Cross-shelf averaged (a) along-shelf velocity, and (b) cross-shelf overturning streamfunction per unit along-shelf distance ($m^2 s^{-1}$), taken at y = 0 km across the western shelf averaged into the annual forcing period.

upwelling (0.5 < t < 1 yr). The mass balance on the shelf forms the basis for a theoretical model of the exchange between the marginal sea and the open ocean in the following section.

There is an exchange between the marginal sea and the open ocean forced by the winds within the marginal sea. Figure 6a shows the meridional transport per unit depth

integrated across the strait. When the wind stress curl in the marginal sea is cyclonic (0 < t < 0.5 yr; Fig. 6d), fluid is being expelled from the basin in the upper ocean and drawn into the basin in the deeper ocean. When there are anticyclonic winds and Ekman pumping within the basin, near-surface waters are drawn into the basin and deeper waters are advected out of the basin. The net transport through the strait at all

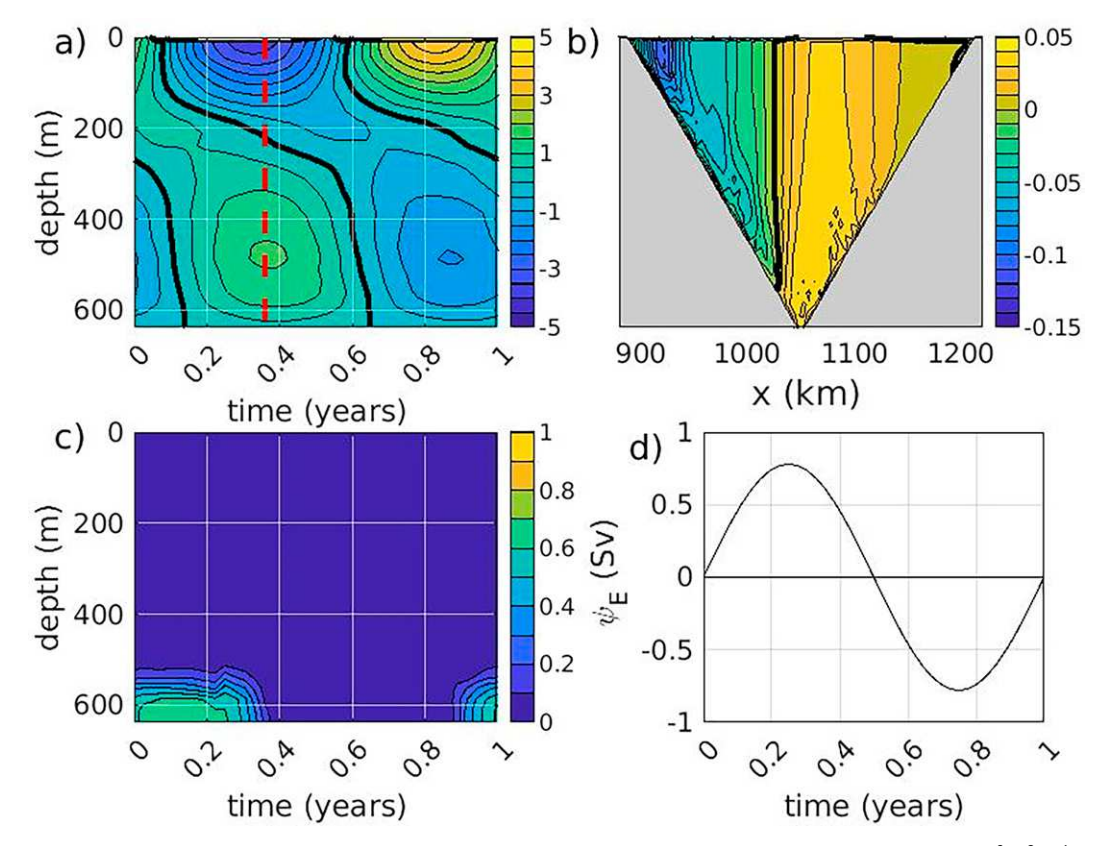


FIG. 6. (a) Average onto a forcing period of the meridional transport through the strait per unit depth $(10^3 \text{ m}^2 \text{ s}^{-1})$. (b) Meridional velocity across the strait at the time of maximum exchange (m s⁻¹). (c) Deep basin tracer at the center of the strait averaged onto the forcing period. (d) Ekman pumping integrated over the basin as a function of time. The thick black lines in (a) and (b) are the zero contour.

times is nearly zero. Although the integrated exchange is baroclinic, it is achieved by a nearly barotropic flow over shallow topography and a nearly barotropic flow in the opposite direction through the deep part of the strait, as indicated in Fig. 6b by the meridional velocity on the day of maximum exchange (red dashed line in Fig. 6a). The Ekman transport is evident very close to the surface, but most of the exchange is carried by geostrophic flows below the Ekman layer. The magnitude of this nearly periodic exchange is 0.48 Sv. This represents 61% of the Ekman transport integrated around the basin perimeter, which has an amplitude of 0.78 Sv. This result indicates that while a significant portion of the Ekman pumping in the basin interior is supplied by upwelling/downwelling within the basin, over half of the transport is supplied or exported through the strait. A major objective of the theoretical development in the following section is to understand what controls this partition between internal and external sources/ sinks of mass into the surface Ekman layer.

A passive tracer was initialized with a value of 1 below the sill depth and a value of zero above the sill depth. This tracer was advected and diffused in the same way as temperature and was restored toward its initial profile in the basin interior with a time scale of 90 days. The average annual cycle of the tracer at the center of the strait is shown as a function of depth and time in Fig. 6c. There are pulses of water that originated below sill depth getting pushed out of the basin during the end of the anticyclonic wind anomalies and drawn back in during the early part of the cyclonic wind anomalies. The tracer indicates that over 50% of the outflowing water deeper than 550 m originated below the sill depth. This is required because, on these time scales, the Ekman pumping is not fully attenuated with depth so that, to conserve mass within the region of closed f/h contours, water must upwell or downwell near the boundaries. On longer time scales the Ekman pumping can be halted by lateral eddy fluxes (Marshall and Radko 2003; Manucharyan and Spall 2016) but on seasonal time scales the winds do not have time to displace the isopycnals far enough in the vertical to trigger baroclinic instability (Manucharyan et al. 2016). This also explains the weak Reynolds stresses in the azimuthal momentum budget.

3. Theory and parameter sensitivities

The marginal sea is defined by three distinct regimes: the interior (with closed f/h contours), the shelf (flat region with a solid boundary that extends outside the marginal sea), and the upper slope (with f/h contours that extend outside the marginal sea). Two simple analytic formulations are derived in this section that provide insight into the circulation in and connection between these regions.

a. Interior dynamics

Expressions for the azimuthal and radial velocities can be derived following the approach of Nøst and Isachsen (2003), Isachsen et al. (2003), and Spall (2016). Integrating the depthaveraged linear momentum equations along contours of constant *f/h* produces a balance between the acceleration of the

along-contour velocity, the radial Coriolis term, the bottom stress, and the surface stress:

$$\frac{\partial}{\partial t} \int_{C} \mathbf{u} \cdot d\mathbf{l} + \int_{C} f \mathbf{k} \times \mathbf{u} \cdot d\mathbf{l} + \int_{C} \frac{C_{d} \mathbf{u}}{h} \cdot d\mathbf{l} = \int_{C} \frac{\tau}{\rho_{0} h} \cdot d\mathbf{l}. \quad (4)$$

The depth-averaged horizontal velocity is \mathbf{u} , the along f/h direction is \mathbf{l} , and C is a contour of constant f/h. The second term on the left-hand side is proportional to the net mass flux into the region enclosed by contour C. The magnitude of this term can be estimated relative to the time rate of change term by assuming that the flow along the contour is geostrophic and that the change in sea surface height required to balance the along-contour acceleration is provided by a net flow into or out of the contour. The ratio of the second term to the first term on the left-hand side can be estimated, for circular topographic contours, as $[r/(2L_d)]^2$, where r is the radius of the contour and L_d is the barotropic deformation radius. For regions small relative to the barotropic deformation radius this term is small. For the present model configuration, this ratio is O(0.1) and so the Coriolis term will be neglected.

Equation (4) may be interpreted as a mass balance for the region enclosed by the contour path C between the surface and bottom Ekman layers and the acceleration of the along-contour flow by a weak net mass flux into or out of the enclosed region. If it is assumed the wind stress increases linearly with radius and is periodic in time with frequency ω , $\tau = \gamma r \sin(\omega t)$, then (4) can be solved for the depth-averaged along-contour velocity V as

$$V = \frac{\gamma r}{\rho_0 C_d} \frac{\sin(\omega t + \phi)}{(1 + \alpha^2)^{1/2}},$$
 (5)

where $\alpha = \omega h/C_d$ and $\phi = \tan^{-1}(-\alpha)$. This is the same method as in Spall (2016) but with a different wind stress distribution. The key nondimensional parameter of the system is α , which is the frictional spindown time scale times the forcing frequency. For $\alpha \gg 1$, the system is essentially inviscid and the maximum velocity lags the wind by 90°. For $\alpha \ll 1$, the wind-forced circulation is strongly damped and the velocity is in phase with the wind. Taking a typical bottom drag of 5×10^{-4} m s⁻¹, a forcing period of 1 year, and a bottom depth of 10^3 m gives $\alpha = 0.4$. It is thus expected that the system response to winds will depend on both the frequency of the forcing and the value of bottom drag on seasonal time scales with a slight lag relative to the wind stress curl. This is consistent with the lag seen in the exchange through the strait in Fig. 6.

The along-slope velocity depends linearly on wind stress. The dependence on bottom drag and bottom depth are more complex as represented through α . For $\alpha \ll 1$ the velocity is proportional to C_d^{-1} and independent of topography while for $\alpha \gg 1$, the velocity is independent of C_d and inversely proportional to bottom depth. This is because in the former case the transport is concentrated in the bottom boundary layer while in the later case it is uniformly distributed throughout the water column.

The depth-integrated ageostrophic radial velocity is forced by three terms: the surface Ekman layer; the bottom Ekman

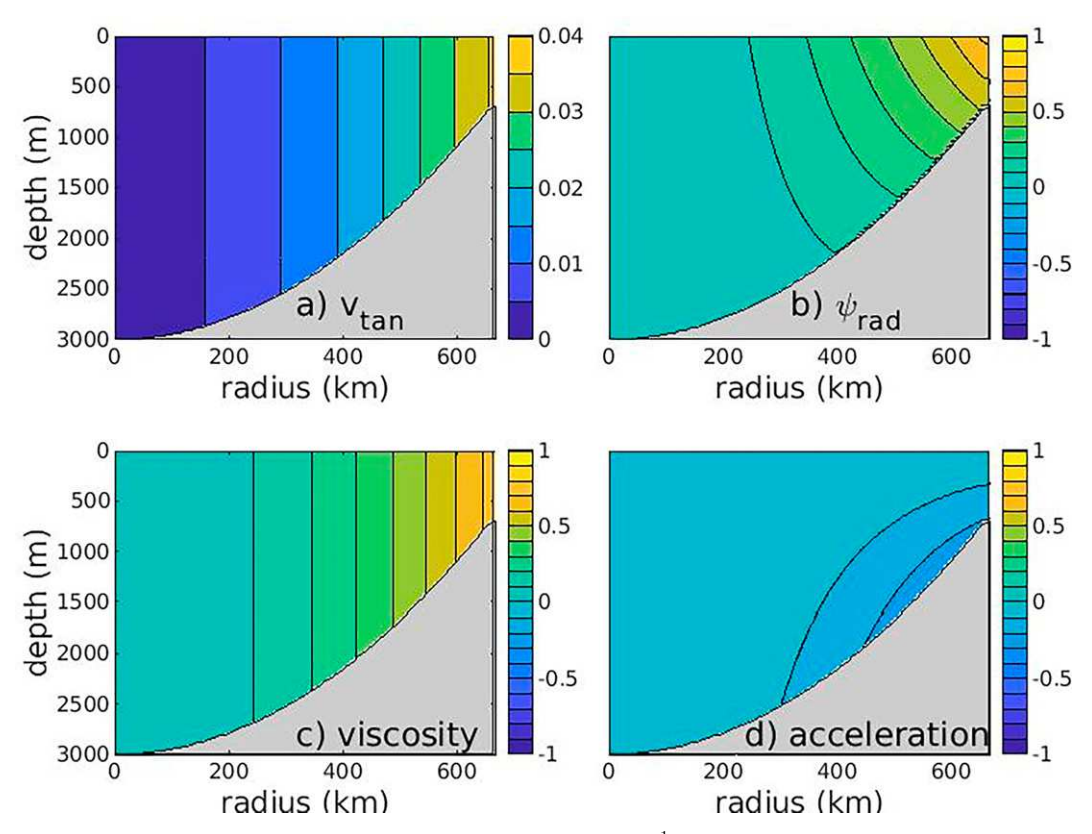


FIG. 7. Theory, (5) and (6), at time = P/4: (a) tangential velocity (m s⁻¹) and (b) radial overturning streamfunction $\psi_{\rm rad}$ (Sv). Also shown are contributions to $\psi_{\rm rad}$ from (c) viscosity and (d) acceleration (Sv).

layer; and the acceleration of the along-contour flow. Away from the Ekman layers, the momentum balance is between the Coriolis term and the along-contour acceleration, yielding

$$U_i = -\frac{1}{f_0} \frac{\partial V}{\partial t} = \frac{\alpha \gamma r}{f_0 \rho_0 h} \frac{\cos(\omega t + \phi)}{(1 + \alpha^2)^{1/2}}.$$
 (6)

The magnitude of the interior radial velocity U_i is proportional to the surface Ekman velocity with a scale factor of

$$\frac{\alpha}{(1+\alpha^2)^{1/2}}\frac{\delta_E}{h},$$

where δ_E is the Ekman layer thickness. For high-frequency forcing relative to the bottom boundary layer spindown time scale ($\alpha \gg 1$), the surface Ekman transport is balanced by a barotropic radial velocity in the opposite direction. For low-frequency forcing ($\alpha \ll 1$), the radial transport is carried primarily in the bottom boundary layer.

The tangential velocity and radial overturning streamfunction calculated from (5) and (6) are shown in Fig. 7 at the time P/4, where P is the forcing period. This is to be compared with the numerical model at 90 days (Fig. 4). The tangential velocity shows a very similar pattern to that found in the numerical model, although the model velocity increases more rapidly at shallow depths. The radial overturning streamfunction also shows a similar pattern with upwelling into the

Ekman layer in the interior being provided primarily by transport out of the bottom Ekman layer (Fig. 7c) but with an inward contribution throughout the water column due to the acceleration of the along-slope flow (Fig. 7d). The mass budget is closed in the theory in infinitely thin surface and bottom Ekman layers.

The fraction of the Ekman transport that is provided through the interior of the water column depends on α . Integrating (6) around the perimeter of the basin and in depth, and scaling by the Ekman transport, provides a simple estimate of how much of the surface Ekman transport is balanced by flow outside the bottom boundary layer:

$$\frac{\psi_i}{\psi_E} = \frac{\alpha}{(1+\alpha^2)^{1/2}}. (7)$$

The interior streamfunction is $\psi_i = 2\pi r h U_i$ and the Ekman transport is $\psi_E = 2\pi r r t/(\rho_0 f_0)$. A series of numerical model calculations was carried out and the radial ageostrophic velocity was diagnosed from the model output. The magnitude of the periodic oscillation in both ψ_i and Ψ_E as a function of radius were diagnosed from the model fields and their maximum ratio is shown in Fig. 8 by the symbols. The theoretical estimate (7) is given by the solid line where, for simplicity, the value of h used to define α is one-half of the maximum bottom depth. Other choices shift the solid line to the right or left on the figure, but the pattern remains the same. In the limit $\alpha \ll 1$,

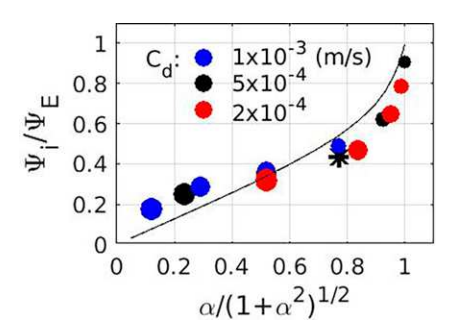


FIG. 8. The portion of the Ekman transport provided by the radial flow outside the bottom Ekman layer as a function of $\alpha/(1 + \alpha^2)^{1/2}$ diagnosed from a series of numerical model runs for different values of bottom drag (colors) and forcing frequency ranging from 1 month to 5 years, with smaller symbols corresponding to shorter periods. The theoretical estimate from (6) is given by the solid line; the asterisk marks the central calculation shown in Fig. 4.

the forcing frequency is low relative to the frictional time scale and the radial transport is contained primarily in the bottom Ekman layer ($\psi_i/\psi_E\ll 1$). As the forcing frequency increases, or friction decreases, α increases and $\alpha/(1+\alpha^2)^{1/2}$ approaches 1. In this limit, all of the Ekman transport is balanced by radial flow in the interior of the water column, outside the bottom Ekman layer. The central case discussed above is given by the asterisk, so at seasonal forcing frequencies a significant portion of the transport is provided in the interior.

b. Shelf dynamics

The dynamic response to surface winds on the shelf is very different from that in the interior for two reasons. First, the shelf extends to a boundary, so the Ekman pumping/suction is concentrated in a very narrow region adjacent to the wall (the winds were designed to have zero Ekman divergence over the shelf). Second, the topographic contours on the shelf extend outside the basin into the external restoring region. Because of this, the approach of integrating along closed *flh* contours used to derive the analytic solutions for the interior is not appropriate for the shelf. Instead, a simple mass balance on the shelf will be used to derive an estimate of the shelf velocity and pressure on the boundary that, it will be shown, controls the exchange between the marginal sea and the open ocean.

Consider a control volume over a section of the shelf starting at the strait and extending in a positive y direction, which is defined as the direction of shelf-wave propagation. The shelf-wave speed is $O(fL_s) = O(10 \text{ m s}^{-1})$ (Brink 2006), which gives an adjustment time scale of O(6 days) over the perimeter of the basin. This is much faster than the forcing time scale, and so it is assumed that mass is balanced over the shelf at all times. At the time depicted in Fig. 9, the wind is upwelling favorable and produces an offshore Ekman transport as indicated by the thin solid arrow. For downwelling favorable winds, the sign of each of the terms is reversed. The pressure anomaly on the boundary on the upstream (in a shelf-wave sense) side of the strait, where y = 0, is set to zero. This is consistent with the focus on circulation and exchange

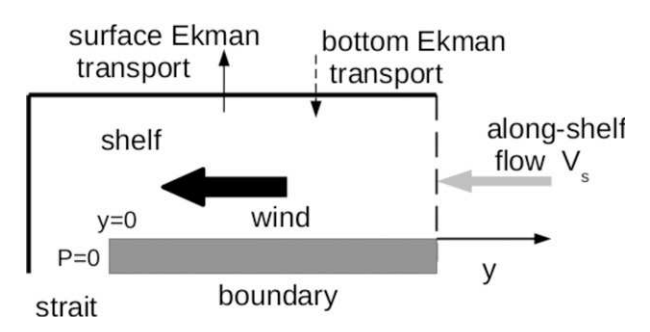


FIG. 9. Schematic of the mass balance on the shelf during upwelling-favorable winds. It is assumed that the pressure at y=0 is zero and that all pressure anomalies are generated from within the marginal sea. There are three contributions to the mass budget: surface Ekman transport, bottom Ekman transport, and along-shelf geostrophic flow.

forced by winds within the marginal sea. One could of course add externally forced variability by specifying a time-dependent value of the pressure at y = 0. The upwelling winds decrease the sea surface height and produce a pressure gradient along the boundary. The resulting cross-shelf pressure gradient is balanced by an along-shelf geostrophic flow, e.g., Allen (1976). Based on the short forcing time scale, the numerical results in Fig. 5, and the theory of Csanady (1978), it is assumed that this along-shelf flow is both barotropic and uniform in the acrossshelf direction. This along-shelf flow produces an onshore transport in the bottom Ekman layer. The scale analysis in the preceding section indicates that the ageostrophic onshore/ offshore flow due to acceleration of the alongshore flow is $O(\omega H_s/C_d) \ll 1$ relative to the bottom boundary layer transport and is generally negligible on the shelf. The mass balance on the shelf is then between the surface Ekman transport, the bottom Ekman transport, and divergence of the along-shelf flow:

$$H_s L_s \frac{\partial V_s}{\partial y} = \frac{\tau_s \sin(\omega t)}{\rho_0 f_0} - \frac{V_s C_d}{f_0},\tag{8}$$

where V_s is the along-shelf velocity, H_s is shelf depth, L_s is the shelf width, and $\tau_s \sin(\omega t)$ is the wind stress over the shelf. In the limit of strong bottom drag ($\alpha \ll 1$), the offshore Ekman transport is balanced by an equal magnitude onshore transport in the bottom boundary layer and the flow $V_s = \tau_s \sin(\omega t)/(\rho_0 C_d)$ and is independent of y. This is the two-dimensional limit in which the flow is not influenced by the strait. In the limit of vanishing bottom drag all of the offshore Ekman transport is provided by the alongshore flow V_s . This is equivalent to the inviscid model of Allen (1976), although the present model does not resolve the cross-shelf structure of the flow.

The solution for the along-shelf velocity is

$$V_{s} = \frac{\tau_{s} \sin(\omega t)}{\rho_{0} C_{d}} (1 - e^{-y/L_{y}}), \tag{9}$$

where $L_y = f_0 L_s H_s / C_d$ is an along-shelf frictional decay scale. This may be interpreted as the distance a shelf-wave would propagate at a wave speed of $f_0 L_s$ over the shelf frictional time

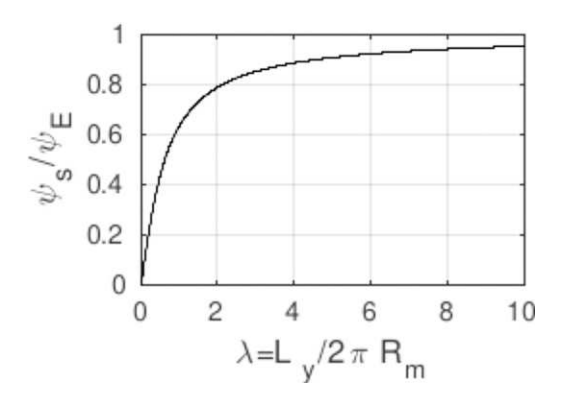


FIG. 10. The ratio of transport through the strait to the interior Ekman transport as a function of the decay scale L_y scaled by the basin perimeter.

scale of H_s/C_d . The transport along the shelf ($\psi_s = H_sL_sV_s$), nondimensionalized by the Ekman transport, is

$$\frac{\psi_s}{\psi_E} = \frac{L_y}{y} (1 - e^{-y/L_y}). \tag{10}$$

The portion of the Ekman transport driven by wind stress in the basin interior that is provided through the open strait depends only on the nondimensional ratio of $\lambda = L_y/(2\pi R_m)$ (Fig. 10). In the limit of strong bottom drag ($\lambda \ll 1$), the alongshelf velocity quickly equilibrates to $V_s = \tau_s \sin(\omega t)/(\rho_0 C_d)$. This drives a bottom Ekman transport that offsets the surface Ekman transport, the flow on the shelf is two-dimensional, and there is only weak along-shelf flow and little exchange through the strait. In the limit of weak bottom drag, such that $\lambda \gg 1$, the along-shelf velocity increases linearly around the perimeter at a rate that provides the transport required to balance the surface Ekman transport, $V_s = \tau_s \sin(\omega t) y/(\rho_0 f_0)$, and all of the transport is provided through the strait.

Assuming the along-shelf flow is barotropic and geostrophic, the change in sea surface height across the shelf is

$$\eta = \eta_0 \sin(\omega t) (1 - e^{-y/L_y}), \tag{11}$$

where

$$\eta_0 = \frac{\tau_s f_0 L_s}{g \rho_0 C_d}.$$

It is assumed that the sea surface height along the offshore side of the shelf is constant in the along-shelf direction, so η represents the change in sea surface height along the outer boundary of the domain. The diagnosed change in sea surface height along the shelf break in the numerical model was found to be small relative to that along the perimeter of the basin (Fig. 3b). However, even the transport implied to cross the shelf break by this small change in sea surface height will remain close to the shelf break. Making use of the vorticity equation of Csanady (1978), the distance any variability in pressure along the shelf break would penetrate into the basin interior scales as $l \propto [yC_d/(f_0s)]^{0.5}$, where y is the distance

around the perimeter of the basin and s is the bottom slope. Taking y as the basin perimeter and a typical bottom slope offshore of the shelf break, l = O(10--30 km). This is much less than the width of the strait and so any flow across the shelf break will remain over the upper slope and flow through the strait. While this effect will shift some of the transport predicted by this simple theory from the shelf onto the upper slope, it will all still pass through the strait, which is the primary diagnostic of interest here.

If (11) is integrated around the perimeter of the basin, the sea surface height on the outflowing side of the strait will be different from the zero anomaly on the inflowing side of the strait. This then requires a surface geostrophic flow into the domain through the strait with transport $gH_s\eta(y=2\pi R_m)/f_0$. Since the mass balance within the marginal sea as a whole must also be satisfied, this exchange along the shelf must be balanced by an opposite directed flow through the deeper part of the strait. Mass is balanced to leading order since the sea surface within the marginal sea is very rigid. For example, a net mass flux into the marginal sea on the order of the Ekman transport, 1 Sv, would cause a 10-m displacement in the ssh over 1 yr. This is prevented by the development of a sea surface height difference between the marginal sea and the open ocean, which drives a barotropic flow through the strait in the opposite direction from the shallow flow onto/off the shelf (e.g., Fig. 6b).

The sea surface height on the boundary adjusts over the along-shelf length scale L_y . For basin perimeters small relative to this length scale, essentially all of the Ekman transport supplied to the interior of the basin is provided by flow through the strait. For basins larger than this length scale, much of the Ekman transport is provided by an overturning within the marginal sea and there is relatively little exchange with the open ocean. For typical parameters of $f_0 = 10^{-4} \, \mathrm{s}^{-1}$, $H_s = 100 \, \mathrm{m}$, $L_s = 100 \, \mathrm{km}$, and $C_d = 5 \times 10^{-4} \, \mathrm{m s}^{-1}$, $L_y = 2000 \, \mathrm{km}$. This is on the same order as the meridional extent of the Nordic Seas and similar in scale to other marginal seas, such as the Japan/East Sea, the South China Sea, the Sea of Okhotsk, the Philippine Sea, and the Mediterranean Sea, suggesting that these shelf dynamics may be important for wind-driven exchange in many marginal-sea settings.

The magnitude of the sea surface height variability along the boundary, relative to that at the inflowing corner of the marginal sea, is shown in Fig. 11a by the solid black line. The black dashed line is an exponential fit to the model data, as in (11), with diagnosed constants $\eta_0=0.037$ m and $L_y=2200$ km. These compare reasonably well to the theoretical estimates of $\eta_0=0.039$ m and $L_y=2000$ km. The other pairs of colored lines correspond to additional calculations in which the bottom drag, shelf width, or shelf depth were varied, each with distinct estimates for η_0 and L_y . Each model calculation results in an approximately exponential profile of the sea surface height along the boundary, consistent with (11).

The along-shelf decay scale diagnosed in the model is compared with L_y predicted by the theory in Fig. 11b. The general linear relationship with $H_s f_0 L_s / C_d$ is found but the model produces a longer decay scale than the theory for small L_y . The sea surface height at the down-wave side of the strait is compared with the theory (11) at $y = 2\pi R_m$ in Fig. 11c. There is

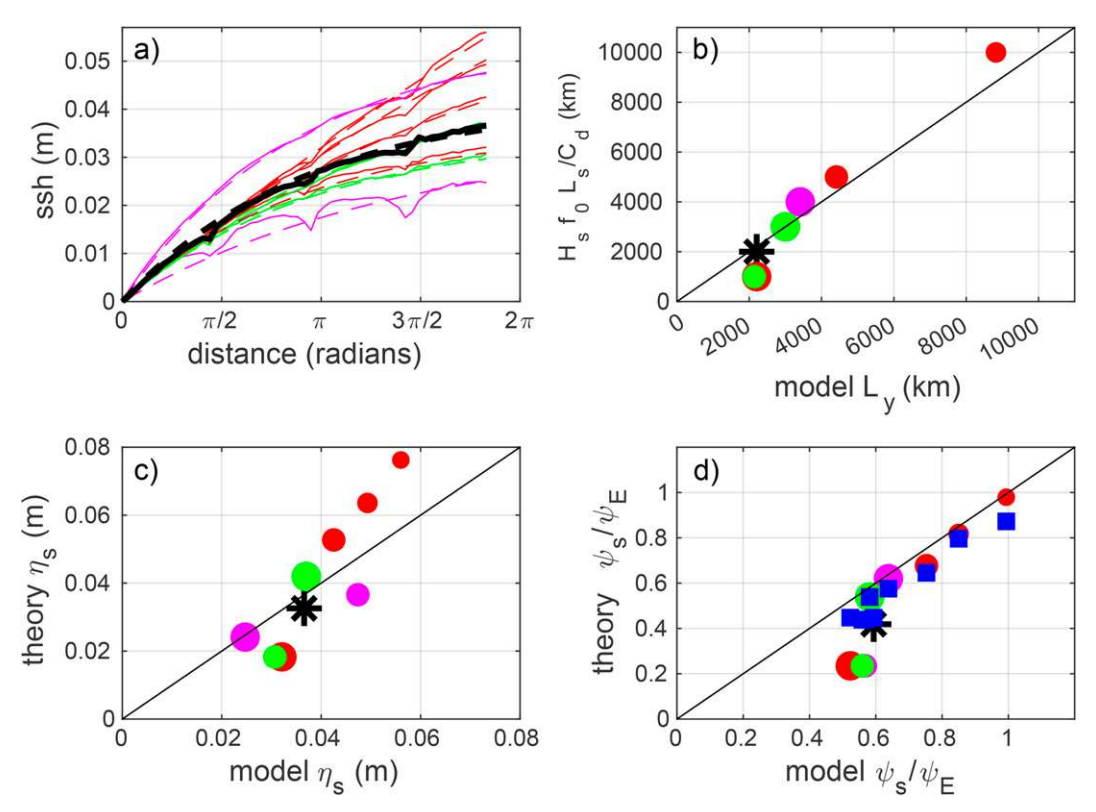


FIG. 11. (a) Amplitude of the sea surface height variability along the boundary for various model parameters. The black line is the central case; red: $C_d=0$, 0.0001, 0.0002, and 0.001; green: $L_s=50$ and 150 km; and magenta: $H_s=50$ and 200 m. The solid lines are diagnosed from the model, and the dashed lines are exponential fits. (b) The along-shelf decay scale L_y diagnosed from the model relative to that predicted by the theory $L_y=H_sf_0L_s/C_d$. (c) The sea surface height anomaly on the down-wave side of the strait diagnosed from the model and predicted by (11). (d) The amplitude of the transport variability through the strait, scaled by the Ekman transport, diagnosed from the model and compared with the theory ψ_s . The colored symbols are based on the theory for L_y , and the blue squares use L_y diagnosed from the model calculations. In (b)–(d), the size of the symbol reflects the magnitude of the relevant parameter.

an approximately linear relationship with the theory predicting a larger height anomaly than that found in the model for small bottom drag (red symbols). The dependence on shelf depth found in the model is weaker than that predicted by the theory.

The amplitude of the variability in the transport through the strait diagnosed from the model is compared with that predicted by $\psi_s = gH_s\eta(y = 2\pi R_m)/f_0$ in Fig. 11d. There is generally good agreement, although the theory underpredicts the transport for strong bottom drag and a narrow shelf. Much of this disagreement is related to the mismatch between the theoretical estimate of the along-shelf decay scale L_{ν} and that found in the model. If L_{ν} diagnosed from the model is used to estimate ψ_s , the agreement is close for all model runs (blue squares). The model runs with low bottom drag and deep or wide shelves produce the largest exchange. For the case with zero bottom drag essentially all of the Ekman transport that is advected into or out of the basin interior is provided from outside the marginal sea and the local overturning within the basin is provided by exchange through the strait. On the other hand, strong bottom drag or narrow, shallow

shelves will isolate the marginal sea from the open ocean and have strong vertical exchange along the boundaries. These shelf dynamics directly influence the deep exchange through the strait because of the basin-scale mass conservation constraint.

c. Upper slope

The region of the upper slope is defined as the region between the depth of the shelf break and the depth of the sill in the strait. This region is complex because, while it follows closed *flh* contours, it also extends outside the marginal sea and into the artificial restoring region. Unfortunately, the restoring region prohibits the use of the approach used to understand the circulation along closed *flh* contours in the interior. It is also not well described by the boundary value approach used for the circulation on the shelf.

The upper slope plays an important role in closing the mass budget of the basin. At the onshore edge of the interior region there is a mass balance between the surface Ekman layer, the bottom Ekman layer, and the interior ageostrophic flow. There is exchange across the shelf edge in the surface and bottom Ekman layers, however, because of the transport provided by the along-shelf flow, the offshore transport in the bottom Ekman layer does not balance the onshore transport in the surface Ekman layer. This results in a mismatch between the radial transport required by the interior and the radial transport provided at the shelf break. The difference is provided by the deep exchange through the strait, which is equal and opposite in sign to the transport along the shelf.

The exact pathway that this transport takes to supply the interior is complicated and not amenable to simple analytic solutions. However, it can be diagnosed in the numerical model and we use the time of maximum cyclonic wind as an example. The flow through the strait into the marginal sea is concentrated over the deepest part of the strait. Just downstream of the strait, this results in too much transport over the deeper contours of the upper slope and too little transport over the shallow contours to balance the surface Ekman transport. The bottom Ekman layer transport over the deep contours, toward the basin interior, is then larger than the surface Ekman layer transport. Conversely, the bottom Ekman layer transport over the shallow upper slope is less than the surface Ekman transport. This mass flux divergence leads to an increase in the sea surface height over the deep contours and a decrease in sea surface height over the shallow contours. The flow adjusts to this change by advecting water from the deep upper slope to the shallow upper slope as it flows cyclonically around the basin. The flow equilibrates when the bottom Ekman layer transport, plus the acceleration term, balances the surface Ekman transport. In the model this occurs approximately one quarter of the way around the basin.

4. Multiple straits

To focus on the underlying dynamics, the analysis so far has considered only a single strait while many marginal seas are connected to the open ocean by more than one strait. In general, the exchange through each strait can be calculated using (10) applied to the segment of coast between each strait, integrating cyclonically around the basin. For basins small relative to L_y the total transport provided from outside the marginal sea will not change, although it will be distributed between straits in proportion to the length of coast upstream of each strait. However, if the basin perimeter is large relative to L_y then the introduction of additional straits will increase the exchange between the marginal sea and the open ocean.

The Nordic Seas has two straits with sills, Denmark Strait and the FBC. They are separated by Iceland, which is O(500) km across and small relative to the perimeter of the Nordic Seas and the typical value of the along-shelf decay scale. Based on the previous analysis, one would expect to see a large wind-driven seasonal exchange through Denmark Strait and a relatively small exchange through the FBC. This is because there is a long coastline with strongly variable winds upstream of Denmark Strait, along the east coast of Greenland, but a short distance along the north coast of Iceland along which sea surface height anomalies could develop and force exchange through FBC. There could also be a recirculation around Iceland forced by winds anywhere along its perimeter.

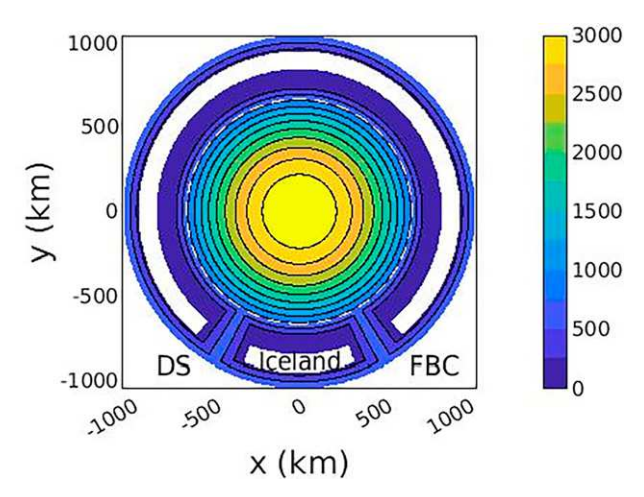


FIG. 12. The model domain and bottom topography (colors). This example consists of a deep basin surrounded by a shallow shelf with two straits with a sill depth of 650 m. The wind stress curl is uniform within the dashed white circle and is zero outside the circle.

The model was run with annual periodic forcing and two straits located along the southern boundary of the model domain (Fig. 12), each with a sill depth of 650 m. In this case there was no restoring in the outer region between the straits. This allows for the development of a recirculation around the island between the two straits. The annual mean cycle of meridional transport per unit depth is shown in Figs. 13a and 13b for the western and eastern straits. Most of the exchange is found in the western strait. This is as expected because the coast upstream of the western strait is much longer (4800 km) than the coast between the two straits (830 km). The alongshelf decay scale is 2000 km, so part of the overturning is provided through the straits and part is within the marginal sea. There is also a barotropic recirculation between the two straits in the same sense as the wind. When the wind stress is cyclonic (0 < t < 0.5P), there is a cyclonic recirculation around the island of strength 0.12 Sv. This causes enhanced southward flow in the upper layer of the western strait and enhanced northward flow in the deep layer of the eastern strait, with the opposite effect for 0.5P < t < P.

If the depth of the eastern strait is increased to 850 m, representative of the deeper Faroe Bank Channel, the dominant upper-ocean exchange remains in the western strait but most of the deep exchange takes place through the eastern strait (Figs. 13c,d). As a result, the barotropic recirculation around the island is now stronger, approximately 0.55 Sv. The exchange on the shelf is now almost entirely through the western strait and the deep exchange is almost entirely through the deeper eastern strait. While this pathway dependence on the difference in sill depths is not considered in the theory, one would expect the barotropic return transport to flow through the deepest strait. This result is consistent with the seasonal cycle found by Jochumsen et al. (2012) and Bringedal et al. (2018), where it was shown that the FBC overflow has a stronger seasonal cycle than does the Denmark Strait overflow. Also, the seasonal cycle in the upper-ocean

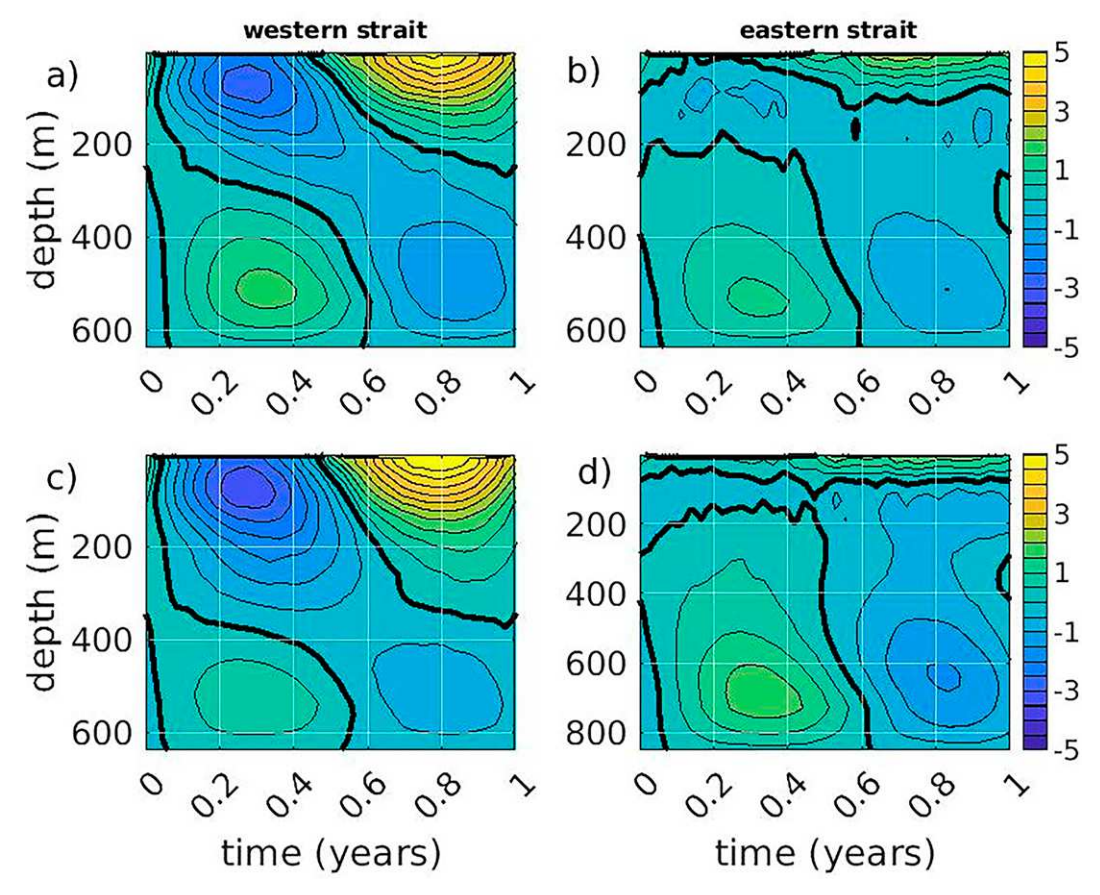


FIG. 13. The meridional transport per unit depth through the western and eastern straits averaged onto a forcing period ($10^3 \text{ m}^2 \text{ s}^{-1}$): the (a),(c) western and (b),(d) eastern straits with (top) equal sill depths of 650 m and (bottom) sill depths of 650 m (west) and 850 m (east).

inflow through Denmark Strait was stronger than the upperocean seasonal cycle through the gateway east of Iceland (Bringedal et al. 2018). The FBC overflow was also in phase with the Denmark Strait inflow while it was phase shifted relative to the FBC inflow. The model and theory predict the FBC overflow and Denmark Strait inflow will be weaker during winter/spring and a stronger during summer/fall. This is also consistent with the findings of Bringedal et al. (2018) and, for the FBC, Chafik et al. (2020). While it is difficult to state with certainty that this observed variability is forced by the winds inside the Nordic Seas, because there is also seasonal forcing outside the marginal sea, the observations are in general agreement with the theory.

5. Discussion and conclusions

The circulation within a marginal sea subject to seasonally varying wind stress curl, and its exchange with the open ocean, were explored using idealized numerical models and analytic theories. The response within regions of closed f/h contours (where f is the Coriolis parameter and h is the bottom depth) is dominated by an oscillating geostrophic flow along the contours and radial ageostrophic flows. The surface

Ekman transport is balanced by the bottom Ekman layer and flow throughout the interior resulting from the acceleration of the azimuthal flow. A simple theory is derived that predicts the azimuthal and radial circulation as a function of a single nondimensional parameter that is the ratio of the spindown time scale and the forcing period. For high-frequency forcing most of the radial transport is carried throughout the water column while for low-frequency forcing most of the radial transport is carried in the bottom boundary layer.

The dynamics on the shelf surrounding the marginal sea were instead shown to be governed by damped shelf waves. The interaction of wind stress with the boundary of the marginal sea introduces a sea surface height gradient along the boundary and a sea surface height differential across any straits connecting the marginal sea to the open ocean. This produces a geostrophic flow on the shelf, out of the marginal sea for cyclonic winds and into the marginal sea for anticyclonic winds. An analytic model for the flow on the shelf shows that the magnitude of this exchange, relative to the Ekman transport, depends on the ratio of the length of the perimeter of the basin and the frictional damping length scale on the shelf. For large basins, most of the Ekman transport into/out of the interior is provided by a local overturning within the marginal sea and

there is little exchange with the open ocean. However, for small marginal seas or short distances between straits most of the Ekman transport is provided by exchange along the boundary through the strait. For typical parameters, this damping length scale is $O(10^3)$ km.

Although the magnitude of this exchange is determined by shelf dynamics, it has a direct influence on the transport of dense waters over the sill. Because mass is conserved within the marginal sea, the flow along the shelf is balanced by an equal amplitude flow through the deep strait in the opposite direction. Numerical model calculations show that some of this deep flow is derived from below the sill depth, so the seasonal winds provide a means to flush the deep marginal sea. The theory predicts a weaker dense overflow in winter/spring and a stronger dense overflow in summer/fall, consistent with the observations of Hansen and Østerhus (2007), Hansen et al. (2015), Chafik et al. (2020), and Bringedal et al. (2018) for the FBC overflow. Bringedal et al. (2018) also find a nearly equal amplitude shallow response through the Denmark Strait that is 180° out of phase with the deep FBC overflow, consistent with the present results.

The main goal of this study was to identify the basic response of a marginal sea to wind stress curl, with an emphasis on how winds within the marginal sea could force exchange with the open ocean. The idealized approach is effective in isolating the controlling physics and identifying the nondimensional parameters that characterize the response. While there are clearly advantages to this idealized framework, relaxing some of the assumptions made here may introduce additional exchange mechanisms. For example, neglect of stratification and variations of the Coriolis parameter with latitude eliminate baroclinic Rossby waves. For forcing periods close to the Rossby wave basin-crossing time scale this will introduce a baroclinic exchange across f/h contours (Spall 2016). This time scale is O(10) years for the Nordic Seas but is only O(1) year for low-latitude marginal seas like the South China Sea. Nonlinearities (Reynolds stresses and eddy thickness fluxes) and buoyancy-forcing are also likely to become important on long time scales while tides may be important on short time scales. Variations in the density change across the sill, which are nearly constant here, were found to be important for the transport through Faroe Bank Channel on both seasonal and interannual time scales by Hansen and Østerhus (2007). It is also not clear how the barotropic exchange through the strait predicted by the present analysis might interact with the baroclinic exchanges through the Denmark Strait and FBC overflow if they are hydraulically controlled. The theory also assumes a simple shelf and slope topography and axisymmetric winds, whereas in reality the winds and topographic slopes vary throughout the marginal sea. While these more realistic configurations do not negate the basic physics identified here, they do make a simple prediction of the response in any marginal sea more difficult.

Acknowledgments. This study was supported by National Science Foundation Grants OCE-1947290, OCE-1922538, and OCE-2218309. This work benefited from conversations

with Dr. Ken Brink and suggestions from two anonymous reviewers.

Data availability statement. Input parameters, data files, and author-modified code for the MITgcm used to produce the central calculation discussed in this paper are available online (https://github.com/michaelspall/Spall-JPO-2022.git).

REFERENCES

- Allen, J. S., 1976: Some aspects of the forced wave response of stratified coastal regions. *J. Phys. Oceanogr.*, **6**, 113–119, https://doi.org/10.1175/1520-0485(1976)006<0113:SAOTFW> 2.0.CO:2.
- Bringedal, C., T. Eldevik, O. Skagseth, M. A. Spall, and S. Osterhus, 2018: Structure and forcing of observed exchanges across the Greenland–Scotland Ridge. *J. Climate*, 31, 9881–9101, https://doi.org/10.1175/JCLI-D-17-0889.1.
- Brink, K., 2006: Coastal-trapped waves with finite bottom friction. Dyn. Atmos. Oceans, 41, 172–190, https://doi.org/10.1016/j. dynatmoce.2006.05.001.
- Chafik, L., H. Hatun, J. Kjellsson, K. Margretha, H. Larsen, T. Rossby, and B. Berx, 2020: Discovery of an unrecognized pathway carrying overflow waters toward the Faroe Bank Channel. *Nat. Commun.*, 11, 3721, https://doi.org/10.1038/s41467-020-17426-8.
- Csanady, G. T., 1978: The arrested topographic wave. *J. Phys. Oceanogr.*, **8**, 47–62, https://doi.org/10.1175/1520-0485(1978)008 <0047:TATW>2.0.CO;2.
- Hansen, B., and S. Østerhus, 2007: Faroe Bank Channel overflow 1995–2005. *Prog. Oceanogr.*, 75, 817–856, https://doi.org/10. 1016/j.pocean.2007.09.004.
- —, K. Larsen, H. Hátún, and S. Østerhus, 2015: A stable Faroe Bank Channel overflow 1995–2015. *Ocean Sci.*, **12**, 1205– 1220, https://doi.org/10.5194/os-12-1205-2016.
- Helfrich, K. R., 1995: Time-dependent two-layer hydraulic exchange flows. J. Phys. Oceanogr., 25, 359–373, https://doi.org/10.1175/1520-0485(1995)025<0359:TDTLHE>2.0.CO;2.
- —, and L. J. Pratt, 2003: Rotating hydraulics and upstream basin circulation. *J. Phys. Oceanogr.*, 33, 1651–1663, https://doi.org/10.1175/2383.1.
- Hersbach, H., 2020: The ERA5 global reanalysis. *Quart. J. Roy. Meteor. Soc.*, **146**, 1999–2049, https://doi.org/10.1002/qj.3803.
- Isachsen, P. E., J. H. LaCasce, C. Mauritzen, and S. Häkkinen, 2003: Wind-driven variability of the large-scale recirculating flow in the Nordic Seas and Arctic Ocean. J. Phys. Oceanogr., 33, 2534–2550, https://doi.org/10.1175/1520-0485(2003) 033<2534:WVOTLR>2.0.CO;2.
- Jochumsen, K., D. Quadfasel, H. Valdimarsson, and S. Jónsson, 2012: Variability of the Denmark Strait overflow: Moored time series from 1996–2011. J. Geophys. Res., 117, C12003, https://doi.org/10.1029/2012JC008244.
- Kamenkovich, V. M., 1962: On the theory of the Antarctic Circumpolar Current. Tr. Inst. Okeanol., 56, 245–306.
- Köhl, A., R. H. Kase, and D. Stammer, 2007: Causes of changes in the Denmark Strait Overflow. J. Phys. Oceanogr., 37, 1678–1696, https://doi.org/10.1175/JPO3080.1.
- Manucharyan, G., and M. A. Spall, 2016: Wind-driven freshwater buildup and release in the Beaufort Gyre constrained by mesoscale eddies. *Geophys. Res. Lett.*, 43, 273–282, https://doi. org/10.1002/2015GL065957.

- —, and A. F. Thompson, 2016: A theory of the wind-driven Beaufort Gyre variability. *J. Phys. Oceanogr.*, **46**, 3263–3278, https://doi.org/10.1175/JPO-D-16-0091.1.
- Marshall, J., and F. Schott, 1999: Open-ocean convection: Observations, theory, and models. *Rev. Geophys.*, 37, 1–64, https://doi.org/10.1029/98RG02739.
- —, and T. Radko, 2003: Residual-mean solutions for the Antarctic Circumpolar Current and its associated overturning circulation. *J. Phys. Oceanogr.*, **33**, 2341–2354, https://doi.org/10.1175/1520-0485(2003)033<2341:RSFTAC>2.0.CO;2.
- —, C. Hill, L. Perelman, and A. Adcroft, 1997: Hydrostatic, quasi-hydrostatic, and non-hydrostatic ocean modeling. *J. Geophys. Res.*, **102**, 5733–5752, https://doi.org/10.1029/96JC02776
- Nøst, O. A., and P. E. Isachsen, 2003: The large-scale time-mean ocean circulation in the Nordic Seas and Arctic Ocean estimated from simplified dynamics. *J. Mar. Res.*, 61, 175–210, https://doi.org/10.1357/002224003322005069.
- Nurser, A. J. G., and S. Bacon, 2013: Eddy length scales and the Rossby radius in the Arctic Ocean. *Ocean Sci. Discuss.*, 10, 1807–1831, https://doi.org/10.5194/osd-10-1807-2013.

- Pratt, L. J., 1997: Hydraulically drained flows in rotating basins. Part II: Steady flow. *J. Phys. Oceanogr.*, **27**, 2522–2535, https://doi.org/10.1175/1520-0485(1997)027<2522:HDFIRB> 2.0.CO:2.
- —, and J. Whitehead, 2008: Rotating Hydraulics. Springer, 582 pp. Smagorinsky, J., 1963: General circulation experiments with the primitive equations: I. The basic experiment. Mon. Wea. Rev., 91, 99–164, https://doi.org/10.1175/1520-0493(1963)091 <0099:GCEWTP>2.3.CO;2.
- Spall, M. A., 2004: Boundary currents and water mass transformation in marginal seas. *J. Phys. Oceanogr.*, 34, 1197–1213, https://doi.org/10.1175/1520-0485(2004)034<1197:BCAWTI>2.0.CO:2.
- ——, 2016: Wind-driven flow over topography. J. Mar. Res., 74, 229–248, https://doi.org/10.1357/002224016820870657.
- Straneo, F., 2006: On the connection between dense water formation, overturning, and poleward heat transport in a convective basin. J. Phys. Oceanogr., 36, 1822–1840, https://doi.org/10.1175/JPO2932.1.
- Whitehead, J., A. Leetma, and R. A. Knox, 1974: Rotating hydraulics of strait and sill flows. *Geophys. Fluid Dyn.*, 6, 101–125, https://doi.org/10.1080/03091927409365790.